Nonparaxial Mie Theory of Image Formation in Optical Microscopes and Characterization of Colloidal Particles

F. Gómez,[1] R.S. Dutra,[2] L.B. Pires,[1] Glauber R. de S. Araújo,[3] B. Pontes,[4,5] P.A. Maia Neto,[1,5] H.M. Nussenzveig,[1,5] and N.B. Viana[1,5,*]

[1] *Instituto de Física, Universidade Federal do Rio de Janeiro, Rio de Janeiro, RJ 21941-972, Brazil*
[2] *LISComp-IFRJ, Instituto Federal de Educação, Ciência e Tecnologia, Rua Sebastião de Lacerda, Paracambi, RJ 26600-000, Brazil*
[3] *Instituto de Biofísica Carlos Chagas Filho, Rio de Janeiro, RJ 21941-901, Brazil*
[4] *Instituto de Ciências Biomédicas, Universidade Federal do Rio de Janeiro, Rio de Janeiro, RJ, 21941-902, Brazil*
[5] *CENABIO—Centro Nacional de Biologia Estrutural e Bioimagem, Universidade Federal do Rio de Janeiro, Rio de Janeiro, RJ, 21941-902, Brazil*

(Received 5 December 2020; revised 28 February 2021; accepted 30 April 2021; published 4 June 2021; corrected 9 June 2021 and 29 June 2021)

We derive an explicit partial-wave (Mie) series for the image of a dielectric microsphere collected by a typical infinity-corrected microscope. We model the propagation of the illumination and scattered vector fields through the optical components of the microscope by using the angular-spectrum theorem with the help of Wigner rotation matrix elements, allowing us to identify the contribution from spin-orbit helicity reversal. We consider a high numerical aperture objective well beyond the validity range of the paraxial approximation. The spherical aberration introduced by refraction at the planar interface between the sample and the glass slide is fully taken into account. By comparing our theoretical model with images of colloidal particles placed at different positions with respect to the objective focal plane, we characterize their radii and refractive index. We employ polystyrene microspheres with a known refractive index in order to fit the transverse attenuation length describing the transmission loss of the scattered field. As an application, we measure the radius and refractive index of individual silica beads. We compare the result for the radius with an independent measurement using high-resolution scanning electron microscopy. To validate the result for the refractive index, we develop a second method, independent of the theoretical model, based on the image contrast in glycerin-water solutions. In all cases we find very good agreement between our method and the validation procedures. In addition, the nonparaxial theory provides a reliable description of the images found for all focal-plane positions and for both polystyrene and silica microspheres. Our approach allows a common optical microscope to be used to measure the refractive index and radius of spherical particles covering the entire size range from the Rayleigh regime to the ray optics one.

DOI: 10.1103/PhysRevApplied.15.064012

I. INTRODUCTION

Light microscopy has undergone considerable advances in recent decades. The attained limit of resolution has reached the nanometric scale by the development of techniques such as confocal scanning [1–3], near field [4,5], structured illumination (SIM) [6], stimulated emission depletion (STED) [7], photoactivated localization (PALM) [8], tracking of fluorescent molecules with minimal photon fluxes (MINFLUX) [9], defocusing [10–12], and stochastic optical reconstruction microscopies (STORM) [13]. Recently, a multifocus strategy has been implemented for three-dimensional (3D) volumetric imaging [14]. Many among the above referred techniques employ imaging of fluorescent markers that allow for nanometric resolution but also require probe attachment that may change the sample. On the other hand, label-free microscopy techniques such as quantitative phase imaging (QPI) use transmitted light microscopy with minimum sample damage but relatively poor molecular specificity and image resolution [15]. Nano-optics [16] has employed the conceptual and theoretical framework of classical and quantum optics to study the available microscopy technologies, and to propose developments based on modern microscope designs. In such a context, accurate theoretical descriptions of the light interaction with samples and microscope lenses are sorely needed.

Methodologies that combine optical microscopy with Mie-scattering theory have been used to track and/or characterize individual colloidal particles, by measuring

*nathan@if.ufrj.br

their refractive index, radius [17–21], and porosity [22], as well as the rotational dynamics of nonspherical particles [23] and the antibodies' binding rate and concentration in solution [24]. A model for light propagation through the optical microscope considering the objective and tube lens as a single effective lens was recently proposed [25].

In this work, we develop a nonparaxial vectorial model based on Mie-scattering theory to describe the interaction between the incident light and a dielectric microsphere, also on the angular-spectrum method to propagate the resulting total field through the optical system. The propagation of the light field through the microscope objective and tube lenses are analyzed separately with the help of the angular-spectrum theorem [16,26]. The refraction through the planar water-glass interface and the resulting spherical aberration [27] are also fully taken into account. We represent the spherical waves scattered by the microsphere as a partial-wave (Mie) series, which is then expanded as a superposition of plane waves by employing Weyl's representation [28,29]. We derive an explicit representation for the light-intensity pattern captured by a CMOS camera in terms of integrals over the aperture angle of the objective lens. The (Mie) scattered fields are represented in terms of Wigner rotation matrices, which allows for an explicit identification of the spin-orbit [30,31] helicity reversal contribution.

Finally, we apply our model to characterize colloidal particles. To accurately describe the experimental results, we introduce two phenomenological parameters describing the attenuation of the light field as it propagates through the optical system. We analyze the images of polystyrene (PS) and silica microspheres to determine their radii. We compare the results with the value provided by the manufacturer for the monodisperse polystyrene microspheres. In the case of the silica microspheres, we use high-resolution scanning electron microscopy to measure the radius, in order to compare with the results obtained by our method. We also measure the refractive index of silica microspheres, and to validate the results we develop a second methodology based on the variation of the image contrast with the dilution of glycerin in aqueous solution, which is employed as the host medium. We find agreement between our method and independent validation procedures in all cases, showing that the proposed theoretical model provides an accurate description of the light-intensity patterns measured in bright-field optical microscopy.

II. NONPARAXIAL THEORY OF THE IMAGE OF A MICROSPHERE ILLUMINATED BY A PLANE WAVE

Our theoretical approach is based on Mie-scattering theory, which we develop in terms of Debye potentials [32]. By using Weyl's integral representation [28,29,33,34] and Wigner rotation matrix elements, we expand the scattered field as a superposition of plane waves. We then proceed by considering the propagation of each plane-wave component across the microscope optical system, which we assume to be infinity corrected. We start by considering the case of coherent illumination, and later introduce an attenuation factor to account for partial transverse coherence of our light source. Our assumptions provide an accurate description of our images obtained with light-emitting-diode (LED) illumination when the condenser aperture diaphragm is partially closed. We also model the transmission loss of the illumination field by introducing a heuristic reduction factor.

We consider the microscope illumination field as a monochromatic plane wave (angular frequency ω and vacuum wavelength $\lambda_0 = 2\pi c/\omega$) propagating in the aqueous host medium (refractive index n_1) along the z direction. We start assuming a linearly polarized wave along the x direction:

$$\mathbf{E}_{\text{in}}(z,t) = E_0 e^{i(k_1 z-\omega t)}\hat{\mathbf{x}}, \tag{1}$$

with $k_1 = n_1\omega/c = 2\pi n_1/\lambda_0$ (c = speed of light in vacuum). In the final steps of our derivation, we take an average of the intensity over all possible directions of polarization in order to model the case of nonpolarized light.

In Appendix A, we solve the Mie scattering by the microsphere imaged by the microscope taking $\mathbf{E}_{\text{in}}(z,t)$ as the incident field. We expand the scattered field in the aqueous host medium as a superposition of circularly polarized plane waves (helicity $= \sigma$):

$$\begin{aligned}\mathbf{E}_s^{(1)}(\mathbf{r}) = -\frac{E_0}{8\pi}\sum_{\sigma=-1,+1}\sum_{J=1}^{\infty}(2J+1)\int_0^{2\pi}d\beta\int_C d\alpha\,\sin\alpha \\ \times\left[a_J g^J_{\sigma,+}(\alpha,\beta)+b_J g^J_{\sigma,-}(\alpha,\beta)\right] \\ \times(\hat{\boldsymbol{\vartheta}}+i\sigma\hat{\boldsymbol{\varphi}})e^{i\mathbf{k}_1(\alpha,\beta)\cdot\mathbf{r}}.\end{aligned} \tag{2}$$

Here, a_J and b_J are the Mie coefficients [35] representing the scattering amplitudes for electric and magnetic multipoles, respectively. They are functions of the microsphere radius a and refractive index n_2, as well as of the index n_1 of the aqueous host medium (see Fig. 1). The direction of the wave vector $\mathbf{k}_1(\alpha,\beta)$ is defined by the spherical angles in the aqueous solution α and β, to which we associate the unitary vectors $\hat{\boldsymbol{\vartheta}}$ and $\hat{\boldsymbol{\varphi}}$, respectively. The integration contour C for the angular variable α, defined in Appendix A, is such as to include both evanescent and propagating waves. However, only part of the evanescent sector contributes by frustration at the water-glass interface when considering propagation through the optical system as detailed below. We define the coefficients:

$$g^J_{\sigma,\epsilon}(\alpha,\beta) = e^{i\sigma\beta}d^J_{\sigma,\sigma}(\alpha) - \epsilon e^{-i\sigma\beta}d^J_{-\sigma,\sigma}(\alpha), \tag{3}$$

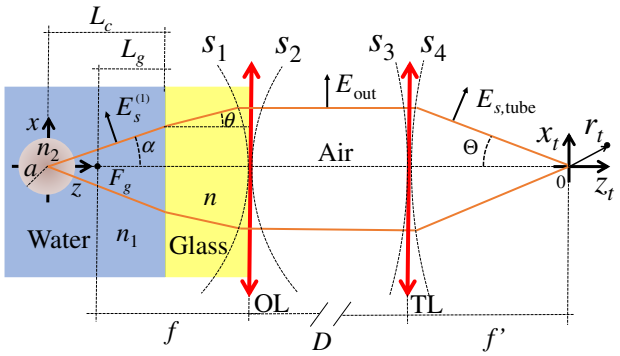

FIG. 1. Propagation of the field scattered by a dielectric microsphere (radius a) through the microscope optical train. The scattering angle α in the host aqueous medium is related to the angle θ in the glass medium by Snell's law of refraction. OL (focal length f) and TL (focal length f') are the objective and tube lenses. The distance D between them satisfy $D = f + f'$. $S_1 - S_4$ are spherical reference surfaces as defined by the sine condition. We calculate the total electric energy density at a point $\mathbf{r}_t$ in the image space of TL.

with $\epsilon = 1(-1)$ for electric (magnetic) multipoles. The matrix elements of finite rotations $d^J_{M',M}(\alpha)$ [36] are taken at $M = M' = \sigma$ for the helicity-conserving terms, and at $M = -M' = \sigma$ for the contribution of the spin-orbit [30] helicity reversal [31] upon Mie scattering.

In Appendix B, we analyze the propagation of the scattered field, Eq. (2), through the optical system as illustrated by Fig. 1. We first consider the refraction at the planar interface separating the aqueous solution from the glass slide of refractive index n. We obtain the refracted field in terms of the angle of refraction $\theta = \sin^{-1}(N \sin\alpha)$ and the corresponding Fresnel coefficient:

$$T(\alpha) = \frac{2N\cos\alpha}{N\cos\alpha + \cos\theta}, \tag{4}$$

with $N = n_1/n$. Refraction also gives rise to the spherical aberration phase [37],

$$\Phi_{g-w}(\theta) = k\left(-L_g\cos\theta + NL_c\cos\alpha\right), \tag{5}$$

where $k = n\omega/c$ is the wave number in the glass medium. As indicated in Fig. 1, L_g and L_c denote the positions of the objective Gaussian focal point and microsphere center, respectively, with respect to the interface.

We use the angular-spectrum theorem and the method of parallel transport when considering transmission across the objective (focal length f) and tube lens (focal length f'). The objective NA defines the nonparaxial opening angle $\theta_0 = \sin^{-1}(\mathrm{NA}/n)$ in the glass medium. Only propagating modes are considered in the glass medium. However, the angular spectrum within the interval $\sin^{-1}(n_1/n) < \theta < \theta_0$ arises from frustration of the microsphere's near field when NA $> n_1$ (which is the case in our experiment). We assume that the objective lens satisfies the Abbe sine condition [32]. As $f' \gg f$, we take the paraxial approximation in the image space of the tube lens.

The propagation of the illumination field, Eq. (1), is derived by the same approach. After crossing the objective lens, the illumination beam is focused at its back focal point, which is placed at the focal plane of the tube lens as the distance between the lenses is $D = f + f'$. We model the total propagation loss of the illumination field, as it propagates from the light source to the image space of the tube lens, with the help of a real transmission amplitude t_{in}. The total field at a point (in cylindrical coordinates) $\mathbf{r}_t(\rho_t, \phi_t, z_t)$ in the image space of the tube lens is then written as

$$\mathbf{E}_{\mathrm{tube}}(\mathbf{r}_t) = \mathbf{E}_{s,\mathrm{tube}}(\mathbf{r}_t) + E_{\mathrm{in,tube}}(\mathbf{r}_t)\hat{\mathbf{x}}. \tag{6}$$

We take the origin at the tube lens back focal point, as illustrated by Fig. 1. The scattered field in the image space of the tube lens $\mathbf{E}_{s,\mathrm{tube}}$ is derived in Appendix B, whereas the illumination field reads

$$E_{\mathrm{in,tube}}(\mathbf{r}_t) = -\frac{t_{\mathrm{in}}E_0 f}{f'}\frac{2n_1}{n_1+n}e^{i(k_1L_c - kL_g)}e^{ik_0(f'+D)}e^{ikf}\,e^{ik_0z_t}, \tag{7}$$

with $k_0 = \omega/c$.

After taking the squared modulus of the total field, Eq. (6), to find the total electric energy density, we average over the azimuthal coordinate ϕ_t as the illumination beam is unpolarized. We find

$$\begin{aligned} I_{\mathrm{tube}}(\rho_t, z_t) &= \frac{1}{2\pi}\int_0^{2\pi} |\mathbf{E}_{\mathrm{tube}}(\rho_t, \phi_t, z_t)|^2 d\phi_t \\ &= |E_{s1}(\rho_t, z_t) + E_{\mathrm{in,tube}}(z_t)|^2 + |E_{s2}(\rho_t, z_t)|^2. \end{aligned} \tag{8}$$

Here, we define the scattered-field amplitudes:

$$\begin{aligned} E_{s1}(\rho_t, z_t) = \frac{E_0}{2}\frac{f}{nf'}e^{ikf}\,e^{ik_0(D+f'+z_t)}\sum_{J=1}^{\infty}(2J+1)(a_J + b_J) \\ \times \int_0^{\theta_0} d\theta \sin\theta d^J_{1,1}(\alpha)J_0\left(k_0\frac{f}{f'}\rho_t\sin\theta\right)t(\theta), \end{aligned} \tag{9}$$

$$\begin{aligned} E_{s2}(\rho_t, z_t) = \frac{E_0}{2}\frac{f}{nf'}e^{ikf}\,e^{ik_0(D+f'+z_t)}\sum_{J=1}^{\infty}(2J+1)(a_J - b_J) \\ \times \int_0^{\theta_0} d\theta \sin\theta d^J_{1,-1}(\alpha)J_2\left(k_0\frac{f}{f'}\rho_t\sin\theta\right)t(\theta), \end{aligned} \tag{10}$$

in terms of the complex transfer amplitude:

$$t(\theta) = \frac{\cos^{3/2}\theta}{\cos\alpha} T(\alpha)\tau(\theta) e^{i\Phi_{g-w}(\theta)} e^{-ik_0 z_t (f^2/2f'^2)\sin^2\theta}. \tag{11}$$

Partial coherence is taken into account in Eq. (11) through the phenomenological factor

$$\tau(\theta) = e^{-(f^2\sin^2\theta/\ell^2)}, \tag{12}$$

where ℓ denotes the transverse attenuation length for the scattered field as it propagates through the optical system, as discussed in more detail in Appendix B.

The amplitude E_{s2} accounts for the spin-orbit helicity reversal $\sigma \to -\sigma$ upon Mie scattering. Its integral representation, Eq. (10), contains the Bessel function [38] $J_2(n_1 k_0 \rho \sin\alpha)$ capturing the nonparaxial spin-orbit coupling driven by Mie scattering at large angles, where $\rho = [f/(nf')]\rho_t$ is the radial distance in the object space of the objective lens. The spin-orbit amplitude E_{s2} vanishes along the beam axis and is maximized at a distance $\rho \sim \lambda_0/n_1$. Equation (10) also shows that the spin-orbit effect arises from the difference between electric and magnetic scattering amplitudes. As a consequence, the effect is subdominant when considering particles that nearly match the refractive index of the host medium, which is the case of the PS and silica microspheres considered in the present paper. On the other hand, the contribution arising from E_{s2} becomes more relevant for particles with larger refractive indices.

In the next section, we use Eqs. (7)–(11) as our theoretical model for the microsphere image and then determine the transverse attenuation length for the scattered field ℓ and the illumination field loss t_{in} as fitting parameters. Whereas the former is a property of the optical system only, the latter also depends on the imaged microsphere as it takes into account the extinction associated to Mie scattering. We determine the attenuation length ℓ by comparing the predictions of our model, Eq. (8), with images of a calibrated PS microsphere. Then we apply the known value of ℓ to measure the refractive index and diameter of silica microspheres. In addition, we assume that the CMOS detector is placed at the back focal plane of the tube lens and then take $z_t = 0$ in Eq. (8). In our model, the real and positive parameters ℓ and t_{in} have clear physical meanings. Their fitted values discussed below are within the range one could expect on physical grounds. Moreover, we verify that the transverse attenuation length ℓ, which accounts for partial transverse coherence of the illumination beam, decreases as a function of the radius of the condenser diaphragm as expected. When employing high-NA oil-immersion objectives, Eq. (12) could also account for the nonuniform transmittance of the objective lens [39], although our comparison between the values of ℓ obtained with different radii of the condenser diaphragm indicates that partial coherence is the dominant effect even in our setup with NA = 1.4. Overall, the introduction of the attenuation factor, Eq. (12), paves the way for implementations of quantitative characterization methods [17–22] using common optical microscopes with LED illumination instead of coherent light sources.

III. MATERIALS AND METHODS

A. Samples

We employ PS [nominal radius $a = (1.50 \pm 0.07)$ μm] and silica [nominal radius $a = (2.50 \pm 0.15)$ μm] microspheres (Polysciences, Inc., USA) in solutions containing distilled water and glycerin $C_3H_5(OH)_3$ (VETEC-Sigma-Aldrich, Brazil). Prior to the experiments, a rubber ring (diameter = 1 cm and height = 2 mm) is attached to a cleaned glass coverslip of dimensions $24 \times 60 \times 0.17$ mm^3 (Knittel, Germany) with the help of silicon grease. A volume of 0.2 μl of the manufacturer's microsphere solution (approximately 10% v/v) is then placed inside the rubber ring together with 160 μl of the aqueous solution (either pure water or glycerin-water). Another glass coverslip, of dimensions $24 \times 32 \times 0.17$ mm^3 (Knittel, Germany), is used to cover the sample, which is then taken to the microscope. To measure the refractive index of silica microspheres, we use glycerin-water samples with increasing glycerin concentrations, from pure water to pure glycerin with concentration steps of 10% v/v.

B. Experimental setup

The samples are observed in a Nikon Ti-S infinity-corrected microscope equipped with a Plan Apo 60X, NA 1.4 oil-immersion objective (Nikon, Japan) and a LED illumination system (470 nm, FWHM 25 nm, M470L3, Thorlabs, USA) adjusted with the Köhler illumination technique. To increase the spatial coherence of the illumination, we close the condenser aperture diaphragm to a diameter of 4 mm in all experiments. We choose a microsphere attached to the glass coverslip in the microscope field of view. We employ the piezoelectric positioning stage E-710 (Physik Instrumente, Germany) to displace the sample and the system focus from -5 to $+5$ μm relative to the in-focus image position with a controlled speed of 0.1 μm/s. Images of the entire process are recorded by an Orca-Flash 2.8 CMOS camera (C11440, Hamamatsu, Japan) with an exposure time of 80 ms and analyzed with the help of ImageJ (U.S. National Institutes of Health, Bethesda, Maryland, USA), Kaleidagraph (Synergy Software, USA) and Mathematica (Wolfram Research, Inc., USA) software packages.

C. Light-intensity contrast and camera gray level

The Orca-Flash 2.8 camera allows to capture 8-bit (256 levels) or 12-bit (4096 levels) gray images. Besides, it

TABLE I. Gray level at zero intensity: values of B [see Eq. (13)] for different combinations of the camera setting parameters.

	8 bits	12 bits
BIN 1	3	51
BIN 2	12	204

operates with two spatial resolution modes, corresponding either to 1920×1440 pixels (BIN 1) or to 960×720 pixels (BIN 2). Using a power meter, we verify that the relationship between the gray level (G) and the light intensity (I) reaching the camera sensor is linear:

$$G = A\,I + B, \tag{13}$$

where A and B are (usually constant) parameters related to the camera settings for gain and black level, respectively [10]. When comparing with our theoretical model, the relevant experimental quantity is the image intensity contrast defined as $C = (I - I_0)/I_0$, where I_0 is the background intensity. Using Eq. (13), we find

$$C = \frac{G - G_0}{G_0 - B}, \tag{14}$$

where G_0 is the gray level corresponding to the image background. Equation (14) shows that image contrast depends strongly on the camera black level B. We determine B for each combination of the camera setting parameters by turning off the microscope illumination system. The resulting values are presented in Table I.

D. Image contrast

After selecting a microsphere image, its center is determined by the ImageJ center-of-mass algorithm. We develop an ImageJ macro to measure the gray level along a straight line crossing through the image center and parallel to the x axis. The line goes from -4.5 μm (left of center) to $+4.5$ μm (right of center) for the 3-μm PS microspheres; and from -6.0 to $+6.0$ μm for the 5-μm silica microspheres. In theory, the gray-level map would be uniform along a circumference centered at the origin. However, we observe variations of approximately 10% that we attribute to an asymmetry of the LED illumination and, to a lesser extent, to a residual misalignment between the microsphere center and the optical z axis. In order to average out such variations, we take consecutive rotations of the probe line by 10° around the z axis. We repeat the gray-level measurement procedure for each of the 18 resulting lines on the x-y image plane. The combined data for a given distance ρ to the image center is averaged, and the image contrast C is determined from Eq. (14).

E. Theoretical model parameters and fitting procedure

Several input parameters are required for the comparison between the theoretical results of Sec. II and the measured image contrasts. We take the refractive-index values (at $\lambda_0 = 470$ nm) $n = 1.5169$ for the glass slide (low-index borosilicate glass [40]) and $n_2 = 1.615 \pm 0.001$ for the PS microspheres (using the dispersion relation given by Ref. [41]). For distilled water we use $n_1 = 1.3383 \pm 0.0002$ [42] with the error bar accounting for room-temperature variation. The refractive index of the silica microspheres is determined by the curve-fitting procedure described below.

Additional parameters include the focal length of tube lens $f' = 20$ cm (valid for Nikon microscopes) and the objective NA $= 1.4$ and focal length $f = nf'/M \approx 0.5$ cm, where $M = 60$ is the objective magnification. The amount of spherical aberration introduced by refraction at the water-glass interface is controlled by L_c and L_g (see Fig. 1). As the microsphere is attached to the glass slide, we take $L_c = a$. We are able to control the position of the objective focal plane L_g (with respect to the interface) by displacing the microscope stage along the z axis with the help of our piezoelectric nanopositioning system, as discussed in Sec. III B.

We develop a Mathematica code to implement the curve fitting by the theoretical intensity function defined by Eqs. (8)–(11). Experimental data corresponding to three different observation planes are simultaneously fitted by the resulting theoretical function taken with the same common set of parameters. The unweighted fitting procedure is implemented by a Mathematica code employing the NonlinearModelFit command to minimize

$$\chi^2 = \sum_i [C_i^{\rm exp} - C^{\rm teo}(\rho_i)]^2, \tag{15}$$

where the sum runs over all experimental points, with a tolerance of 10^{-6}. To achieve the desired tolerance, up to 500 iterations are performed. The runtime for each contrast curve is approximately 2 h when using a computer with an IntelCore i7-5500U processor. A Mathematica code for the numerical evaluation of the contrast as a function of the radial coordinate is provided as Supplemental Material [43].

For PS microspheres, the fit parameters are the initial value of L_g, written in terms of the dimensionless quantity $\mathcal{L}_0 = L_g/a$, the microsphere radius a, and the two parameters describing transmission loss: the attenuation length ℓ for the scattered field and the global transmission amplitude $t_{\rm in}$ for the illumination field. We collect images at the initial (reference) position corresponding to $\mathcal{L}_0$ as well as at two additional vertical sample positions, which are obtained by applying a known displacement ΔL_g from the reference position. We then take a global fit of all images assuming a common set of parameters $(\mathcal{L}_0, a, \ell, t_{\rm in})$ (with

$L_g = a\mathcal{L}_0 + \Delta L_g$ for the additional images). In addition, we also carry out independent fits of the individual images for each vertical position of the sample in order to compare the results with the global fit.

For the silica microspheres, we replace ℓ (which is determined from the data for PS) by the microsphere refractive index n_2. Note that the value for the parameter t_{in} in the silica experiment is not expected to coincide with the value found for the PS case as t_{in} is also connected to extinction by Mie scattering.

F. Refractive index of silica microspheres: glycerin method

As a validation of our method for the determination of the refractive index n_2 of our silica microspheres, we implement a second, independent method for measuring the refractive index. As n_2 lies in between the values for the refractive indices of water and glycerin ($n_{\text{gly}} \approx 1.48$) [44], it is possible to tune the concentration of glycerin in aqueous solution so as to match the microsphere refractive index.

We analyze the intensity contrast of silica microspheres immersed in water-glycerin solutions at different concentrations using a high magnification optical microscope. Our method relies on the rule that the image intensity contrast reaches a minimum at the condition of index matching as the absorption of silica is negligibly small in the visible range [$\text{Im}(n_2) \approx 7 \times 10^{-8}$ at $\lambda_0 = 470$ nm [45]].

We obtain a Cauchy dispersion formula for each value of glycerin concentration [gly] by employing a mercury lamp and measuring the minimum angle of deviation by an optical water-glycerin prism. We then use the results to obtain the refractive index of each of our samples at $\lambda_0 = 470$ nm. A linear relation between the refractive index of water-glycerin solutions ($n_{\text{WG}}^{(470\text{ nm})}$) and glycerin concentration [gly] is found:

$$n_{\text{WG}}^{(470\text{ nm})} = (1.3315 \pm 0.0007) + (1.495 \pm 0.009) \times 10^{-3}[\text{gly}]. \quad (16)$$

We prepare a sample of silica microspheres in water-glycerin solution, as described in Sec. III A, and take it to the microscope. As in the procedure employed for the samples containing pure water (see Sec. III B), we displace the sample using the piezoelectric stage from 5 μm below to 5 μm above the in-focus sphere image, collecting 1250 images at a rate of 12.5 Hz. We obtain the intensity contrast for each image pixel with the help of standard ImageJ tools, calculate the contrast squared for each pixel, and then the integral of the squared contrast over a disk (radius $a_d = 5.30\ \mu\text{m} \approx 2a$) concentric with the sphere image. We then compare the squared contrast over the several contrast maps corresponding to different sample vertical positions to find the minimum integrated squared contrast ($\mathcal{M}$):

$$\mathcal{M} = \left[2\pi \int_0^{a_d} d\rho\rho C(\rho)^2\right]_{\text{min}}. \quad (17)$$

For each glycerin concentration we find a given value for $\mathcal{M}([\text{gly}])$ as defined by Eq. (17). This procedure is repeated 5 times for each one of the 11 concentrations employed in the experiment. The function $\mathcal{M}([\text{gly}])$ has a minimum at the concentration $[\text{gly}]_{\text{min}}$, which is determined by a quadratic fit in the close neighborhood of the minimum. The uncertainty of $[\text{gly}]_{\text{min}}$ is evaluated by a quadratic error propagation of the fit confidence intervals carried out with Kaleidagraph, which minimizes χ^2 while weighting data with the inverse of the squared error. Finally, we determine the refractive index of the silica microsphere by substituting $[\text{gly}]_{\text{min}}$ into Eq. (16).

G. High-resolution scanning electron microscopy (HSEM)

A diluted sample with ultrapure water Milli-Q®(Merck Millipore) with silica microspheres (1:100) are adhered to 12-mm-diameter round glass coverslips (Paul Marienfeld GmbH & Co. KG, Germany) previously coated with 0.01% poly-L-lysine (Sigma-Aldrich, Darmstadt, Germany) for 20 min, and dried using a low-pressure argon jet. The specimen is mounted on stubs using a conductive carbon adhesive (Pelco Tabs™, Stansted, Essex, UK). Samples are sputter coated with a 4–5-nm-thick platinum layer using a Leica EM SCD 500 sputtering device (Wetzlar, Germany). Considering the high Young modulus of polystyrene and silica we do not expect changes in the sphere morphology due to sample preparation. Finally, secondary electron images (SEIs) are obtained in a Quanta 450™ FEG (FEI Company, Oregon, USA) scanning electron microscope, at an accelerating voltage of 5.0 kV.

IV. RESULTS

A. Images of polystyrene and silica microspheres

For PS spheres, we initially place the objective focal plane (red) near the glass slide ($\mathcal{L}_0 \ll 1$) as illustrated by Fig. 2(a). The resulting reference image, shown in Fig. 2(d), contains a maximum at the center surrounded by a bright ring with a comparable intensity. Valuable information on the probe particle can be obtained by moving the optical system out of focus [10,11]. Images for two additional focal-plane positions are recorded by displacing the piezoelectric nanopositioning stage downward, so as to move the focal plane up into the sample region. We take the displacements $\Delta L_g = 1.5\ \mu$m [Figs. 2(b) and 2(e)] and $\Delta L_g = 3.0\ \mu$m [Figs. 2(c) and 2(f)] from the initial reference position shown in Fig. 2(a). The entire procedure is repeated with three different microspheres from the

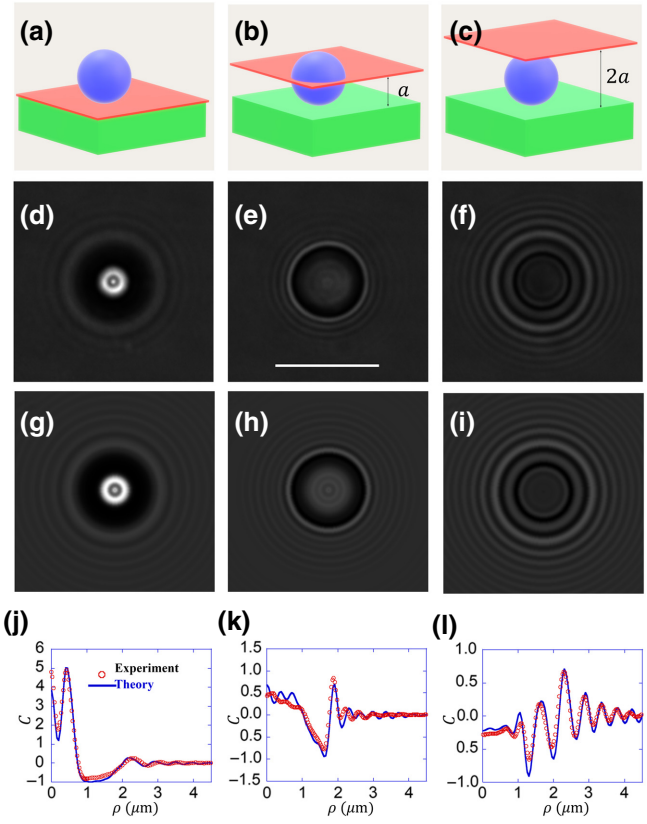

FIG. 2. From left to right, the image of the polystyrene particle (attached to the glass slide) is brought out of focus by driving the microscope stage downwards. As a consequence, the objective focal plane (red) is displaced upwards with respect to the glass slide, as illustrated by (a)–(c). The corresponding experimental and simulated images are shown in (d)–(f) and (g)–(i), respectively. Plots of the theoretical (line) and experimental (circles) image contrast versus the distance to center ρ are shown in (j)–(l). The scale is the same for all images and is indicated by a horizontal bar (5 μm) in (e).

same batch. The resulting nine images are processed into intensity contrast maps and the global fitting implemented as described in Sec. III. Fitting contrast curves obtained from multiple focal planes with the same set of parameters provides compelling evidence that the proposed theoretical model accurately describes the main physical ingredients of our experiment. Nevertheless, our methodology can also be carried out by analyzing a single plane, which might be preferable for several applications. To simulate such a procedure, we also fit each of the nine contrast curves separately in the case of PS. In both situations we estimate the error bars as the standard deviation. The results are summarized in Table II. Figures 2(g)–2(i) show the simulated images for each focal-plane position taking the parameters obtained from the global fit. In Figs. 2(j)–2(l), we plot the theoretical contrast versus the cylindrical coordinate ρ (solid line) as calculated from the global fitting as well as the experimental data (circles).

TABLE II. Fitting parameters employed in the nonparaxial theory of the image of a dielectric microsphere. $\mathcal{L}_0$ is the initial position of the focal plane with respect to the glass slide (in units of radius), a is the microsphere radius, $t_{\rm in}$ is the transmission loss for the incident field, ℓ is the transverse attenuation length for the scattered field, and n_2 is the microsphere refractive index. In the case of polystyrene, we took the dispersion formula of Ref. [41] to calculate n_2. PS stands for results obtained from the global fit of the three different focal plane positions with a common set of parameters, while PS* denotes the average of results obtained from independent fits for each individual plane. As ℓ is a characteristic length of the microscope alone, it should not depend on which particle is imaged. Thus, the value found for ℓ in the PS experiment was employed when computing the theoretical image of the silica microspheres.

	PS	PS*	silica
$\mathcal{L}_0$	-0.078 ± 0.007	-0.068 ± 0.004	-0.69 ± 0.02
a (μm)	1.4821 ± 0.0005	1.47 ± 0.02	2.32 ± 0.01
ℓ (cm)	0.47 ± 0.02	0.44 ± 0.06	–
$t_{\rm in}$	0.466 ± 0.007	0.47 ± 0.01	0.498 ± 0.004
n_2	–	–	1.428 ± 0.002

We follow the same global fitting protocol discussed in the previous paragraph when considering silica microspheres. The reference image is shown in Fig. 3(d), again with a central intensity maximum surrounded by a bright ring with a similar contrast. However, now the corresponding focal-plane position turns out to be well below the glass slide as illustrated by Fig. 3(a). Two additional focal-plane positions are obtained by taking $\Delta L_g = 2.43$ μm [Figs. 3(b) and 3(e)] and $\Delta L_g = 4.86$ μm [Figs. 3(c) and 3(f)]. We use the value for the transverse attenuation length found in the PS experiment and take $\mathcal{L}_0$, a, $t_{\rm in}$, and n_2 as fitting parameters. We repeat the procedure for three silica microspheres. The resulting values for the fitting parameters are shown in Table II. Figures 3(g)–3(i) show simulated images obtained with the fitting parameters. Figures 3(j)–(l) show the best-fit theoretical intensity contrast (solid line) as well as the measured contrast (circles) as functions of ρ.

B. Refractive index of silica microspheres from the glycerin method

Figure 4 summarizes the results of the glycerin experiment intended for an independent characterization of the refractive index of silica microspheres (see Sec. III F for details). In Fig. 4(a), we plot the $\mathcal{M}$, as defined by Eq. (17), versus concentration. The continuous line corresponds to a smooth curve fit, used here as a guide for the eye, showing that $\mathcal{M}([\text{gly}])$ develops two local minima. The absolute minimum is close to $[\text{gly}] \approx 60\%$. In the inset of Fig. 4(c), we show a quadratic fit for $\mathcal{M}([\text{gly}])$ in the vicinity of the absolute minimum. We weight the error bars to determine the uncertainty. Fitting yields the value $[\text{gly}]_{\rm min} =$

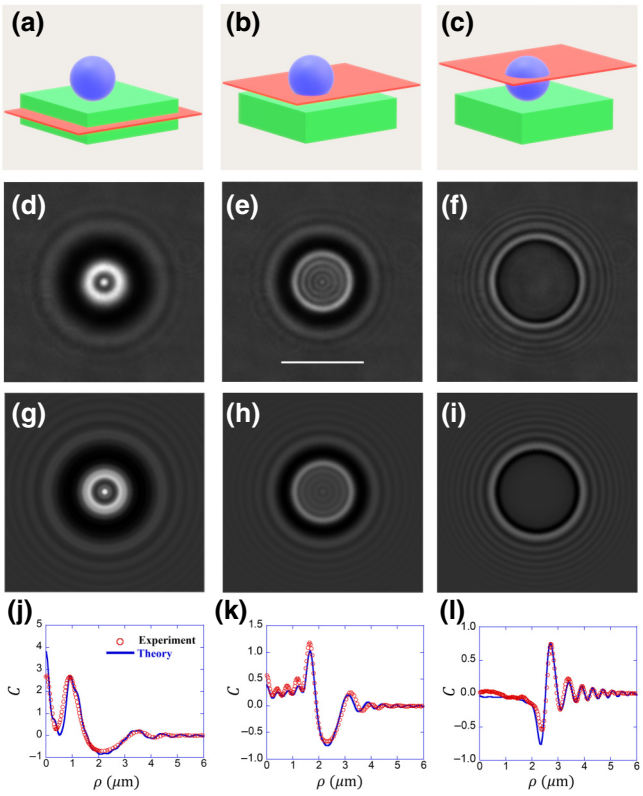

FIG. 3. Images and contrast plots of a silica microsphere attached to the glass slide. Same conventions as in Fig. 2. The scale bar in (e) corresponds to 5 μm also as in Fig. 2. In contrast with Fig. 2, the initial reference image (d) corresponds to a focal-plane position below the glass slide as indicated in (a).

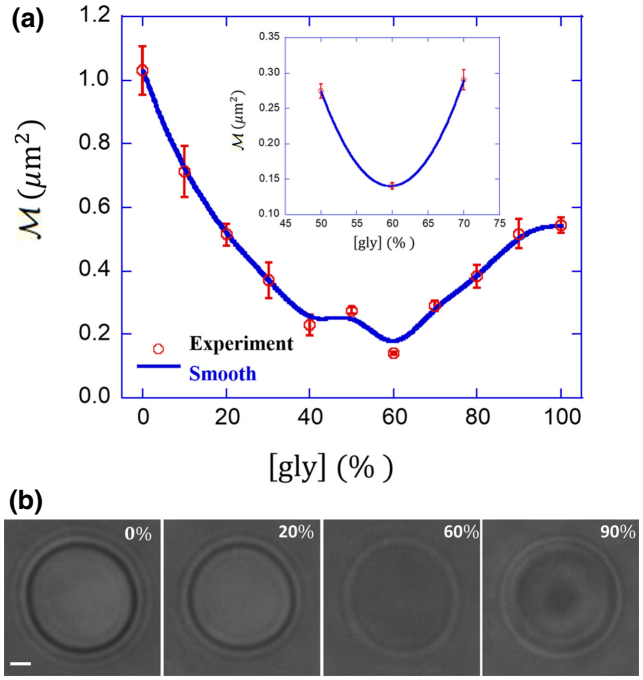

FIG. 4. Glycerin method as an alternative measurement of the refractive index of silica microspheres. (a) Experimental values of $\mathcal{M}$ (circles with error bars) versus glycerin concentration. A smooth fit to the data (solid line) is also shown. Inset: enlargement showing the experimental data and a quadratic fit weighting the error bars for the determination of the concentration $[\text{gly}]_{\text{min}}$, and respective uncertainty. (b) Images of the silica microsphere in pure water and in glycerin-water solutions of 20%, 60%, and 90% concentrations. The images correspond to focal-plane positions such as to minimize the integrated squared contrast as required by the definition of $\mathcal{M}$ [see Eq. (17)]. The scale is the same in all images and is indicated by the scale bar of 1 μm. The refractive index is obtained after substitution of $[\text{gly}]_{\text{min}}$ into Eq. (16).

$(61 \pm 6)\%$ for the point of absolute minimum. Figure 4(b) shows typical images of a silica microsphere immersed in pure water and in a water-glycerin solution with increasing concentrations from left to right (v/v) [gly] = 20%, 60%, and 90%. Note the fading in the panel corresponding to [gly] = 60%, which indicates a condition of near index matching between the microsphere and the solution.

After substituting the value of $[\text{gly}]_{\text{min}}$ into Eq. (16), we find

$$(n_2)_{\text{silica}} = 1.423 \pm 0.009. \tag{18}$$

C. Radius of silica spheres from HSEM

In order to compare with the result for the silica microsphere radius derived from the optical images, we conduct an independent characterization using HSEM images as illustrated by Fig. 5(a) (see Sec. III G for details). In Fig. 5(b), we plot the gray level along the dashed line shown in Fig. 5(a). Figure 5(c) presents an enlarged plot showing the vicinity of one of the edges. In this region, we fit the gray-level data with a hyperbolic tangent function (solid line), so as to determine the position of the edge. The fitting procedure is repeated in the vicinity of the opposite edge. The microsphere diameter is then calculated as the difference between the positions of the edges. The entire procedure is repeated for ten different microspheres that looked similar in shape and size. The microsphere radius is found to be $a_{\text{silica}}^{\text{HSEM}} = (2.35 \pm 0.06)$ μm, considering the standard deviation as the error bar.

V. DISCUSSION

The development of an analytical model that accurately describes the images obtained by an optical microscope can open the way to transform bright-field imaging into a powerful analytical tool. For instance, the morphological and optical properties of colloidal particles are especially relevant when studying these systems. Silica and PS spheres are often used as probes in the study of colloidal forces using optical tweezers [46–48] and total internal reflection microscopy [49]. In those experiments, it is common to employ averaged radii and bulk optical properties

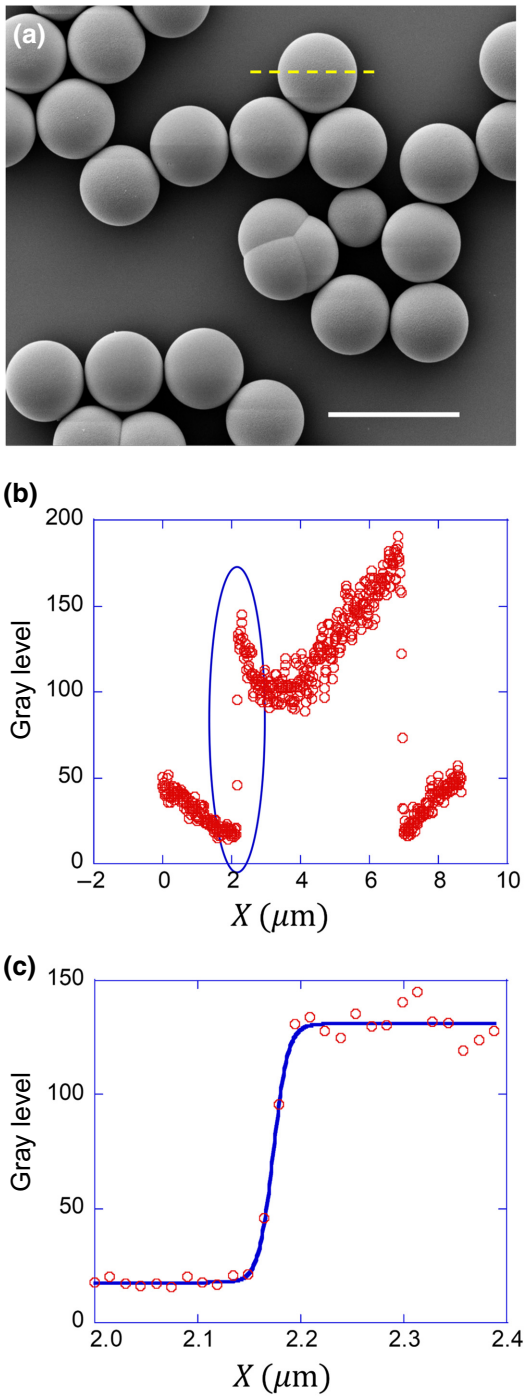

FIG. 5. (a) HSEM image of silica microspheres and (b) gray-level plot along the diameter indicated as a dashed horizontal line in (a). (c) Enlargement of the gray level (circles) in the vicinity of the leftmost edge [highlighted by an ellipse in (b)] and hyperbolic tangent fit (solid line) for the determination of the edge position. The scale bar in (a) corresponds to 8 μm.

in the experimental analysis, which might introduce systematic errors. The bright-field image of a microsphere in a microscope contains information about the sphere radius and complex refractive index (including absorption) at the wavelength of the illumination system. This information can be accessed for each individual microsphere using the nonparaxial image model proposed in this work. For the very transparent materials and moderate particle diameters considered here, absorption is too small to allow for its characterization. However, images of larger polystyrene particles would bring information about the absorption coefficient, thus opening the way for its measurement by following the approach outlined in this work.

A second field of potential applications involve tether extraction experiments, which typically employ micromanipulation tools, such as optical traps [50,51], atomic force microscopy [52], and micropipettes [53] to create a thin cellular membrane tube, also called membrane tether. By measuring the force for tether elongation and the tether radius, the membrane surface tension and bending modulus are characterized. These are relevant membrane elastic properties and have been correlated with several cellular functions [54–56]. Tethers have typical diameters ranging from 50 to 300 nm [54,57–59]. To make a direct measurement of tether radius, confocal microscopy [60] or HSEM [50,56] are usually employed. Both use expensive equipment and require sample fixation. Recently, the diameters of neurites were measured in an optical microscope by combining classical diffraction theory, defocusing and a calibration procedure [12]. However, classical diffraction theory is not expected to provide an accurate description when dealing with structures smaller than the light wavelength. A nonparaxial vector model based on exact solutions for the light-scattering problem would provide a safer ground for applications involving tethers. It would allow for a real-time measurement of the tether radius and refractive index, thus helping to fully characterize the cell-membrane mechanical properties while keeping the cell alive throughout the experiment.

Here we develop a nonparaxial model for the microscope bright-field image of a spherical dielectric object and fit the model parameters to describe images of PS and silica microspheres, allowing measurement of the sphere radius and refractive index. Our model describes the microscope illumination system as a coherent source. In fact, the light emitted by our LED source is only partially coherent. In order to set experimental conditions as close as possible to coherent illumination, we close the aperture of the condenser diaphragm to a diameter of 4 mm, circa one fifth of the full aperture. Partial coherence is taken into account by introducing a Gaussian reduction factor for the propagation of the scattered field. The characteristic transverse attenuation length is found to be $\ell = (0.47 \pm 0.02)$ cm from the analysis of PS microspheres. According to the sine condition, the attenuation increases with the scattering angle. The transmission amplitude falls to $1/e \approx 0.37$ of its maximum value along the forward (axial) direction at the scattering angle $\theta = \sin^{-1}(\ell/f) \approx 59^\circ$, which is slightly smaller than the objective opening angle $\theta_0 =$

$\sin^{-1}(\mathrm{NA}/n) \approx 67^\circ$. When increasing the diameter of the condenser aperture diaphragm (and thus reducing spatial coherence [61]), we observe a reduction of the fitted values for ℓ (data not shown), as expected.

We also introduce a global attenuation factor for the illumination field, t_{in}, describing the total loss associated to propagation from the LED source to the image space of the tube lens. In contrast with the attenuation length ℓ, t_{in} depends on the imaged microsphere, since it is also related to the extinction effect arising from Mie scattering. We find $(t_{\mathrm{in}})_{\mathrm{PS}} = 0.466 \pm 0.007$ and $(t_{\mathrm{in}})_{\mathrm{silica}} = 0.498 \pm 0.004$ for PS and silica microspheres, respectively. Since PS has a larger refractive index, our results are consistent with the larger extinction resulting from Mie scattering by PS microspheres. Another interesting feature revealed by our approach concerns the position of the focal plane. Although the images shown in Figs. 2(d) and 3(d) (for PS and silica microspheres, respectively) are very similar, the corresponding focal heights differ by more than one micron. Each microsphere can be thought as a microlens focusing the incident light into a plane whose position depends strongly on its refractive index and radius. When compared to the polystyrene microsphere, the light focusing by the silica microsphere is observed further downstream, as expected given its smaller index and larger radius. To avoid systematic errors, such microlens effect should be taken into account when using optical images to measure axial displacements.

We implement a global fitting of multiple images with a common set of parameters in order to provide a compelling test of the proposed theoretical model. As an example of application, we measure the radius of the PS microspheres, and the radius and refractive index of silica microspheres. We find $a_{\mathrm{PS}} = (1.4821 \pm 0.0005)\ \mu$m, which is consistent with the value and dispersion range provided by the manufacturer (see Sec. III A). In the Supplemental Material [62] we show a video of experimental (left) and respective simulated (right) images of a polystyrene microsphere [nominal radius $a = (1.50 \pm 0.07\ \mu\mathrm{m})$] as the microscope stage is driven downward along the negative z axis. The focal plane is moving upward with respect to the particle and the total displacement is $\Delta L_g = 5.5\ \mu$m. All simulations are made with the same set of values for the parameters required by the model (see Table II). Note the similarity between real and simulated images for all focal-plane positions relative to the microsphere, demonstrating the accuracy of our model. The residual disagreement between theory and experiment is mainly in the close neighborhood of the image center, particularly when the position of the microsphere relative to the focal plane is such as to concentrate the intensity near the central region. Since our theoretical approach already includes near-field contributions, such residual difference might be attributed to multiple reflections between the microsphere and the glass-water interface, which should be more relevant when considering the vicinity of the sphere-glass contact point.

For PS microspheres, we also perform separate curve fits of contrast data corresponding to individual focal-plane positions. As shown by Table II, the results from the two fitting procedures agree within error bars. In addition, the average $\chi^2 = 19 \pm 7$ found in the global fit is close to the value $\chi^2 = 14 \pm 5$ obtained by averaging over the individual fits. We conclude that our methodology can also be implemented by fitting a single image, particularly if the focal-plane position is such that the light intensity is not concentrated near the symmetry axis as in Figs. 2(d) and 3(d). Indeed, we confirm that the agreement with the theoretical model is generally worse in this case, as discussed in the previous paragraph, by comparing the values of χ^2 at different focal-plane positions for the same PS microsphere. We find that χ^2 is approximately $10\times$ larger at the reference focal plane position close to the interface [see Figs. 2(a) and 2(j)] when compared to the individual fits for the positions indicated in Figs. 2(b) and 2(c).

We also verify the accuracy of the values found for the distance L_g between the focal plane and the glass surface by comparing the difference between the fitted values obtained for different plane positions with the displacement controlled by the piezoelectric actuator. The single-image fit leads to a systematic error in the determination of the distance L_g, which is underestimated by approximately 6%, while the microsphere radius can be accurately determined from a single image with a percent-level precision.

When simulating the images of silica spheres, we take the value for the transverse attenuation length ℓ obtained from the PS experiment, as this parameter characterizes the microscope optical train and should not depend on the imaged particle. We find $a_{\mathrm{silica}} = (2.32 \pm 0.01)\ \mu$m for the silica microsphere radius, in agreement with the value found by HSEM (see Sec. IV C). For the refractive index, we find $(n_2)_{\mathrm{silica}} = 1.428 \pm 0.002$, which is in agreement with the result of the glycerin method (see Sec. IV B). Although the latter also relies on the image contrast taken at different focal positions, it is fully independent of our theoretical modeling, as required for a genuine validation procedure. The difference between our values and the refractive index of pure fused silica ($n_{\mathrm{silica}} = 1.464$ at $\lambda_0 = 470$ nm [63]) might be attributed to the porosity of our beads and is consistent with recent measurements of the mass of silica microspheres [64].

The discrete dipole approximation (DDA) [23] is also a powerful tool to analyze microscope images, called holograms, obtained by the interference of the illumination and scattered fields, in a similar way as implemented here. The division of the scattering object into small dipoles can be a useful and fast technique in some situations. Our methodology, based on exact analytical results, which can be derived for simple geometries (spheres, cylinders) is

complementary to the DDA method, which is capable of treating more general geometries but is in practice more limited in terms of size range and dielectric properties as the required computational resources generally increase with size and refractive index [65,66]. Within DDA, the lattice parameter of the required dipole grid scales as approximately $\lambda_0/(10n_2)$ [67]. Thus, the number of dipoles is roughly proportional to $(n_2a/\lambda_0)^3$. On the other hand, the Mie-scattering approach is numerically efficient for arbitrary values of refractive index, with the number of required multipoles scaling linearly with a/λ_0, regardless of the value of the particle's refractive index [68].

VI. CONCLUSION

We develop a nonparaxial vector theory of the image of dielectric spherical particles in an optical microscope with a high-NA objective. We combine Mie-scattering theory with the angular-spectrum theorem in order to analyze the propagation of the scattered and illumination field through the microscope optical train. Our approach takes into account the sector of the microsphere's near field that is converted (by frustration at the water-glass interface) into propagating modes within the angular acceptance of the objective. Partial coherence of the illumination field is modeled as a Gaussian attenuation function, associated with a characteristic transverse length ℓ, which depends on the diameter of the condenser aperture diaphragm but not on the particle to be imaged. We also introduce the global reduction factor t_{in} associated to extinction of the illumination beam as it propagates from the LED source until the image space of the tube lens. While ℓ depends only on the optical imaging system, t_{in} also depends on the properties of the imaged particle, as it takes into account extinction due to Mie scattering and absorption. In addition, our theoretical approach highlights the spin-orbit effect in the context of optical microscopy. Although such an effect turns out to be negligible for the microspheres employed in the present paper, its contribution would be relevant for particles with higher refractive indices, as well as in the characterization of chiral particles by adapting methods of circular differential scattering [69] and chiral scatterometry [70].

We employ our model to study images of PS and silica colloidal particles in aqueous solution. We measure their radii and found agreement between our results and the values reported by the manufacturer. As our batch of silica microspheres presented a significant size dispersion, we also measure their radii with high-resolution scanning electron microscopy and find agreement within error bars. As a final application, we characterize the refractive index of the silica beads and compare the result with an independent method based on the condition of index matching with a water-glycerin solution at the appropriate concentration. We again find agreement between the two methods. Our approach can be used to fully characterize colloidal particles, opening the way for measurements of refractive index and sphere radius below the standard resolving limit with a standard bright-field microscope equipped with a LED source. For better results, the transverse attenuation length can be calibrated by employing a microsphere with a known refractive index. When fitting the optical image at a single observation plane, the method allows for a percent-level precision. In this case, the method is optimized by displacing the particle slightly out of focus. A higher precision is attained by fitting multiple images collected at different planes, especially if a piezoelectric nanopositioning system is available. As a perspective, our method can be extended to the cylindrical geometry, which would bring into play useful applications in cell biology, such as, for instance, the real-time characterization of cell-membrane tethers.

ACKNOWLEDGMENTS

The authors are grateful to Ubirajara Agero and Oscar Mesquita for inspiring discussions. We also thank the Instituto Nacional de Metrologia, Qualidade e Tecnologia (Inmetro) for letting us use their high-resolution scanning electron microscope. We acknowledge support from the Brazilian agencies National Council for Scientific and Technological Development (CNPq–Brazil), Coordination for the Improvement of Higher Education Personnel (CAPES–Brazil), the National Institute of Science and Technology Complex Fluids (INCT-FCx), and the Research Foundations of the States of Minas Gerais (FAPEMIG), Rio de Janeiro (FAPERJ) and São Paulo (FAPESP).

APPENDIX A: MIE SCATTERING AND WEYL'S INTEGRAL REPRESENTATION

In this appendix, we recast the standard Mie-scattering theory in a form suitable for considering the propagation through the microscope optical components. As illustrated by Fig. 6, scattering of the illumination field by the microsphere generates spherical waves. We expand the scattered field $\mathbf{E}_s^{(1)}(\mathbf{r})$ in the aqueous medium as a partial-wave series in terms of the electric and magnetic Debye potentials [32] (we omit the time factor $e^{-i\omega t}$):

$$\Pi_s^e(\mathbf{r}) = \frac{E_0}{k_1}\sum_{J=1}^{\infty} i^{J+1}(-a_J)\sqrt{\frac{\pi(2J+1)}{J(J+1)}}h_J^{(1)}(k_1 r) \times [Y_{J,1}(\theta,\phi) - Y_{J,-1}(\theta,\phi)], \tag{A1}$$

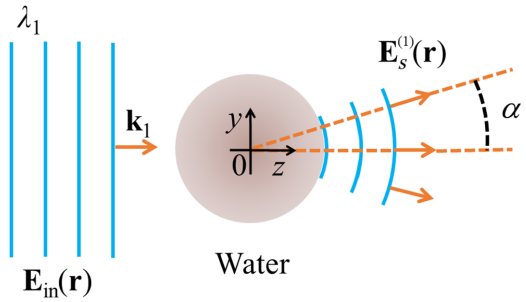

FIG. 6. Scattering of the incident plane wave $\mathbf{E}_{\text{in}}(\mathbf{r})$ (wavelength $\lambda_1 = \lambda_0/n_1$) by a dielectric microsphere centered at the origin of the coordinate system. The scattered field $\mathbf{E}_s^{(1)}(\mathbf{r})$ is expanded as a superposition of plane waves. Each plane-wave component propagates along a direction defined by the scattering angle α (relative to the forward z direction).

and

$$\Pi_s^m(\mathbf{r}) = \frac{H_0}{k_1}\sum_{J=1}^{\infty} i^J(-b_J)\sqrt{\frac{\pi(2J+1)}{J(J+1)}}h_J^{(1)}(k_1 r) \times [Y_{J,1}(\theta,\phi) + Y_{J,-1}(\theta,\phi)]. \quad \text{(A2)}$$

Here, a_J and b_J are the electric and magnetic Mie coefficients [35], respectively, while $Y_{J,M}(\theta,\phi)$ and $h_J^{(1)}(k_1 r)$ denote the spherical harmonics and spherical Hankel functions [38]. The latter corresponds to outgoing spherical waves as illustrated by Fig. 6. We take the origin of our coordinate system at the sphere center and introduce the magnetic field amplitude $H_0 = n_1 E_0/(c\mu_0)$, where μ_0 is the vacuum permeability.

In order to consider the propagation of the scattered field through the optical system, we expand the Debye potentials, Eqs. (A1) and (A2), as a superposition of plane waves. We employ Weyl's integral representation [28,29,33,34] for the product $\Pi_{JM}(\mathbf{r}) \equiv h_J^{(1)}(k_1 r)Y_{J,M}(\theta,\phi)$:

$$\Pi_{JM}(\mathbf{r}) = \frac{i^{-J}}{2\pi}\int_0^{2\pi} d\beta \int_C d\alpha \sin\alpha\, Y_{J,M}(\alpha,\beta)e^{i\mathbf{k}_1\cdot\mathbf{r}}, \quad \text{(A3)}$$

where the direction of the wave vector in the aqueous solution $\mathbf{k}_1 = \mathbf{k}_1(\alpha,\beta)$ is defined by the spherical angles α (depicted in Fig. 6) and β. The integration contour C in the complex plane of the angular variable α contains the interval from 0 to $\pi/2$ along the real axis, followed by the interval from $\pi/2$ to $\pi/2 - i\infty$ running parallel to the negative imaginary axis. C is chosen so as to take into account both evanescent (imaginary values of α) and homogeneous waves that propagate forward into the half-space $z > 0$ ($k_{1z} > 0$). Replacing the representation, Eq. (A3), into Eqs. (A1) and (A2), we find

$$\Pi_s^e(\mathbf{r}) = \frac{ik_1}{2\pi}\int_0^{2\pi} d\beta \int_C d\alpha \sin\alpha\, \Pi_s^e(\alpha,\beta)e^{i\mathbf{k}_1\cdot\mathbf{r}}, \quad \text{(A4)}$$

and

$$\Pi_s^m(\mathbf{r}) = \frac{ik_1}{2\pi}\int_0^{2\pi} d\beta \int_C d\alpha \sin\alpha\, \Pi_s^m(\alpha,\beta)e^{i\mathbf{k}_1\cdot\mathbf{r}}, \quad \text{(A5)}$$

where the electric and magnetic angular spectra are given by

$$\Pi_s^e(\alpha,\beta) = -\frac{E_0}{k_1^2}\sum_{J=1}^{\infty} a_J\sqrt{\frac{\pi(2J+1)}{J(J+1)}} \times [Y_{J,1}(\alpha,\beta) - Y_{J,-1}(\alpha,\beta)], \quad \text{(A6)}$$

and

$$\Pi_s^m(\alpha,\beta) = i\frac{H_0}{k_1^2}\sum_{J=1}^{\infty} b_J\sqrt{\frac{\pi(2J+1)}{J(J+1)}} \times [Y_{J,1}(\alpha,\beta) + Y_{J,-1}(\alpha,\beta)], \quad \text{(A7)}$$

respectively.

From the plane-wave expansions of the Debye potentials, Eqs. (A4) and (A5), we derive the angular-spectrum representation for the scattered electric field:

$$\mathbf{E}_s^{(1)}(\mathbf{r}) = \frac{ik_1}{2\pi}\int_0^{2\pi} d\beta \int_C d\alpha \sin\alpha\, \mathbf{E}_s(\alpha,\beta)e^{i\mathbf{k}_1\cdot\mathbf{r}}, \quad \text{(A8)}$$

where the angular spectrum $\mathbf{E}_s(\alpha,\beta)$ is given by

$$\mathbf{E}_s(\alpha,\beta) = \mathbf{k}_1 \times \mathbf{L}\Pi_s^e(\alpha,\beta) + \frac{c\mu_0}{n_1}k_1\mathbf{L}\Pi_s^m(\alpha,\beta). \quad \text{(A9)}$$

Here, $\mathbf{L} = -i\mathbf{k}\times\nabla_{\mathbf{k}}$ is the orbital angular-momentum operator in reciprocal space.

Substituting Eqs. (A6) and (A7) into Eq. (A9), and then replacing the resulting expression back into Eq. (A8), we obtain the explicit representation Eq. (2) for the scattered field as a superposition of circularly polarized plane waves.

APPENDIX B: PROPAGATION OF THE SCATTERED FIELD THROUGH THE MICROSCOPE OPTICAL COMPONENTS

In this appendix, we analyze the propagation of the scattered field, Eq. (2), through the optical system illustrated by Fig. 1.

1. Propagation across the water-glass interface

We first consider the propagation of the scattered field in the host aqueous medium $\mathbf{E}_s^{(1)}(\mathbf{r})$, Eq. (2), across the planar interface separating the sample from the microscope glass slide (see Fig. 1). For that purpose, it is convenient

to express the angular-spectrum representation, Eq. (2), in terms of Cartesian coordinates in reciprocal space [71]:

$$\mathbf{E}_s^{(1)}(\mathbf{r}) = \int\int dk_{1x}dk_{1y}\mathbf{E}_s^{(1)}(k_{1x},k_{1y},0)e^{i\mathbf{k}_1\cdot\mathbf{r}}, \tag{B1}$$

where the angular spectrum $\mathbf{E}_s^{(1)}(k_{1x},k_{1y},z)$ corresponds to a mixed representation in which the Fourier transform is taken over the x and y spatial coordinates. Here, we take the plane $z=0$, defined by the position of the microsphere center as shown in Fig. 1, and derive the spectrum from Eq. (2):

$$\begin{aligned}\mathbf{E}_s^{(1)}(k_{1x},k_{1y},0) = &-\frac{E_0}{8\pi k_1 k_{1z}}\sum_{\sigma=-1,+1}\sum_{J=1}^{\infty}(2J+1)\\ &\times\left[a_J g_{\sigma,+}^J(\alpha,\beta)+b_J g_{\sigma,-}^J(\alpha,\beta)\right]\\ &\times(\hat{\boldsymbol{\vartheta}}+i\sigma\hat{\boldsymbol{\varphi}}),\end{aligned} \tag{B2}$$

where the spherical angles are now given by $k_{1x}=k_1\sin\alpha\cos\beta$ and $k_{1y}=k_1\sin\alpha\sin\beta$ as functions of the Cartesian variables k_{1x},k_{1y}.

Solving the boundary conditions at the interface separating the sample from the glass slide, we obtain the angular-spectrum representation for the electric field in the glass medium (n), with the origin displaced to the Gaussian focus F_g (see Fig. 1):

$$\mathbf{E}_s(\mathbf{r}) = \int\int dk_x dk_y \mathbf{E}_s(k_x,k_y,0)e^{i\mathbf{k}\cdot\mathbf{r}}. \tag{B3}$$

The angular spectrum in the glass medium is derived from Eq. (B2) and reads

$$\begin{aligned}&\mathbf{E}_s(k_x,k_y,0)\\ &\quad=-\frac{E_0}{8\pi k^2}\sum_{\sigma=-1,+1}\sum_{J=1}^{\infty}(2J+1)\frac{T(\alpha)}{\sqrt{\cos\theta}}\frac{e^{ik_{1,z}L_c}}{\cos\alpha}e^{-ik_zL_g}\\ &\qquad\times\left[a_J g_{\sigma,+}^J(\alpha,\beta)+b_J g_{\sigma,-}^J(\alpha,\beta)\right](\hat{\boldsymbol{\theta}}+i\sigma\hat{\boldsymbol{\phi}}).\end{aligned} \tag{B4}$$

We employ the approximation $T(\alpha)=T_\perp(\alpha)\approx T_\parallel(\alpha)$ for the Fresnel coefficients corresponding to s and p linear polarizations, which is accurate for a water-glass interface. $\hat{\boldsymbol{\theta}}$ and $\hat{\boldsymbol{\phi}}$ are the unitary vectors associated to the spherical angles $\theta=\sin^{-1}(n_1\sin\alpha/n)$ and $\phi=\beta$ in the glass medium, respectively. The Cartesian wave-vector components in the glass medium are

$$k_x = k\sin\theta\cos\phi,\quad k_y = k\sin\theta\sin\phi,\quad k_z = k\cos\theta. \tag{B5}$$

We also introduce the factor $1/\sqrt{\cos\theta}$ in Eq. (B4) to account for the sine condition [16].

2. Propagation across the tube lens

We use the angular-spectrum theorem [26] to connect the angular spectrum $\mathbf{E}_s(k_x,k_y,0)$ at the focal plane of the objective (focal length $=f$) with the field $\mathbf{E}_\infty^s$ at the point of spherical coordinates (θ,ϕ) on the reference spherical surface S_1 (radius f centered at F_g) defined by the sine condition and shown in Fig. 1. We find

$$\mathbf{E}_\infty^s(\theta,\phi) = -2\pi i k_z \mathbf{E}_s(k_x,k_y,0)\frac{e^{ikf}}{f}, \tag{B6}$$

with k_x, k_y, and k_z given by Eq. (B5). We obtain the field at the objective exit port by taking the Kirchhoff approximation and employing the method of parallel transport of the unitary vectors [32]:

$$\mathbf{E}_{\text{out}}(\rho,\phi) = \left\{[\mathbf{E}_\infty^s(\theta,\phi)\cdot\hat{\boldsymbol{\theta}}]\hat{\boldsymbol{\rho}}+[\mathbf{E}_\infty^s(\theta,\phi)\cdot\hat{\boldsymbol{\phi}}]\hat{\boldsymbol{\phi}}\right\}e^{-\rho^2/\ell^2}, \tag{B7}$$

where $\rho=f\sin\theta$ (sine condition), $\hat{\boldsymbol{\rho}}=\cos\phi\hat{\mathbf{x}}+\sin\phi\hat{\mathbf{y}}$, and $\hat{\boldsymbol{\phi}}=-\sin\phi\hat{\mathbf{x}}+\cos\phi\hat{\mathbf{y}}$. Transmission loss and partial coherence are taken into account through the phenomenological factor $e^{-\rho^2/\ell^2}$. Here, ℓ denotes the transverse attenuation length for the scattered field as it propagates through the optical system.

Propagating the field $\mathbf{E}_{\text{out}}(\rho,\phi)$ over the distance D to the tube lens entrance (focal length $=f'$) and using again the method of parallel transport and the angular spectrum theorem, now for the spherical reference surface S_4 shown in Fig. 1, we obtain the angular spectrum at the focal plane of the tube lens:

$$\begin{aligned}&\mathbf{E}_{s,\text{tube}}(k_{0,x},k_{0,y},0)\\ &\quad=\frac{f'e^{ik_0(f'+D)}e^{-\rho^2/\ell^2}}{2\pi i k_{0,z}}\\ &\qquad\times\left\{[\mathbf{E}_\infty^s(\theta,\phi)\cdot\hat{\boldsymbol{\theta}}]\hat{\boldsymbol{\Theta}}+[\mathbf{E}_\infty^s(\theta,\phi)\cdot\hat{\boldsymbol{\phi}}]\hat{\boldsymbol{\phi}}\right\}.\end{aligned} \tag{B8}$$

The azimuthal angle ϕ is conserved when propagating through the optical system, whereas the spherical angle in the image space of the tube lens (see Fig. 1) is given by $\Theta=\sin^{-1}(f/f'\sin\theta)$. $\hat{\boldsymbol{\Theta}}$ denotes the corresponding unitary vector. The spherical angles (Θ,ϕ) in the image space of the tube lens are related to $(k_{0,x},k_{0,y})$ as in Eq. (B5) with the wave number in glass k replaced by the vacuum wave number $k_0=\omega/c$.

The angular spectrum, Eq. (B8), allows us to write the scattered field (after propagation through the optical train) at a point $\mathbf{r}_t(\rho_t,\phi_t,z_t)$ in the image space of the tube lens as a superposition of plane waves. We take the origin at the focus of the tube lens as indicated in Fig. 1. Since $f'\gg f$, we take the paraxial approximation $\Theta\ll 1$

and expand the axial wave-vector component as $k_{0z} \approx k_0\left[1-(f'^2/2f'^2)\sin^2\theta\right]$. Then, we find an explicit integral representation for the scattered field by substituting Eqs. (B4) and (B6) into Eq. (B8):

$$\mathbf{E}_{s,\mathrm{tube}}(\rho_t,\phi_t,z_t) = \sum_{\sigma=-1,+1} E_{s,\sigma}(\hat{\mathbf{x}}+i\sigma\hat{\mathbf{y}}). \tag{B9}$$

The helicity components are given by

$$\begin{aligned} E_{s,\sigma} = {} & \frac{E_0}{4}\frac{f}{nf'}e^{ikf}\,e^{ik_0(D+f'+z_t)}\sum_{J=1}^{\infty}(2J+1) \\ & \times\int_0^{\theta_0} d\theta\left[a_J I^J_{\sigma,+}(\theta)+b_J I^J_{\sigma,-}(\theta)\right]\frac{\sin\theta}{\cos\alpha} \\ & \times\cos^{3/2}\theta\, T(\alpha)e^{i\Phi_{g-w}(\theta)}e^{-(f^2\sin^2\theta/\ell^2)} \\ & \times e^{-ik_0 z_t(f^2/2f'^2)\sin^2\theta}, \end{aligned} \tag{B10}$$

with:

$$\begin{aligned} I^J_{\sigma,\epsilon}(\theta) = {} & d^J_{\sigma,\sigma}(\alpha)J_0\left(k_0\frac{f}{f'}\rho_t\sin\theta\right) \\ & +\epsilon e^{-2i\sigma\phi_t}d^J_{-\sigma,\sigma}(\alpha)J_{2\sigma}\left(k_0\frac{f}{f'}\rho_t\sin\theta\right). \end{aligned} \tag{B11}$$

By substituting Eqs. (B9)–(B11) and Eq. (7) into Eq. (6), we obtain the representation Eqs. (8)–(11) for the electric energy density in the image space of the tube lens.

[1] M. Minsky, Memoir on inventing the confocal scanning microscope, Scanning **10**, 128 (1988).

[2] V. Prasad, D. Semwogerere, and Eric R. Weeks, Confocal microscopy of colloids, J. Phys. Condens. Matter **19**, 113102 (2007).

[3] S. R. Liber, G. Indech, E. B. van der Wee, A. V. Butenko, T. E. Kodger, P. J. Lu, A. B. Schofield, D. A. Weitz, A. van Blaaderen, and E. Sloutskin, Axial confocal Tomography of capillary-contained colloidal structures, Langmuir **33**, 13343 (2017).

[4] D. W. Pohl, W. Denk, and M. Lanz, Optical stethoscopy: Image recording with resolution $\lambda/20$, Appl. Phys. Lett. **44**, 651 (1984).

[5] A. Lewis, M. Isaacson, A. Harootunian, and A. Muray, Development of a 500 Å spatial resolution light microscope: I. Light is efficiently transmitted through $\lambda/16$ diameter apertures, Ultramicroscopy **13**, 227 (1984).

[6] M. G. L. Gustafsson, Surpassing the lateral resolution limit by a factor of two using structured illumination microscopy, J. Microsc. **198**, 82 (2000).

[7] S. W. Hell and J. Wichmann, Breaking the diffraction resolution limit by stimulated emission: Stimulated-emission-depletion fluorescence microscopy, Opt. Lett. **19**, 780 (1994).

[8] E. Betzig, G. H. Patterson, R. Sougrat, O. W. Lindwasser, S. Olenych, J. S. Bonifacino, M. W. Davidson, J. Lippincott-Schwartz, and H. F Hess, Imaging intracellular fluorescent proteins at nanometer resolution, Science **313**, 1642 (2006).

[9] K. C. Gwosch, J. K. Pape, F. Balzarotti, P. Hoess, J. Ellenberg, J. Ries, and S. W. Hell, MINFLUX nanoscopy delivers 3D multicolor nanometer resolution in cells, Nat. Methods **17**, 217 (2020).

[10] U. Agero, C. H. Monken, C. Ropert, R. T. Gazzinelli, and O. N. Mesquita, Cell surface fluctuations studied with defocusing microscopy, Phys. Rev. E **67**, 051904 (2003).

[11] U. Agero, L. G. Mesquita, B. R. A. Neves, R. T Gazzinelli, and O. N. Mesquita, Defocusing microscopy, Microsc. Res. Tech. **65**, 159 (2004).

[12] M. Anthonisen, Y. Zhang, M. H. Sangji, and P. Grütter, Quantifying bio-filament morphology below the diffraction limit of an optical microscope using out-of-focus images, Appl. Opt. **59**, 2914 (2020).

[13] M. J. Rust, M. Bates, and X. Zhuang, Sub-diffraction-limit imaging by stochastic optical reconstruction microscopy (STORM), Nat. Methods **3**, 793 (2006).

[14] S. Xiao, H. Gritton, H.-A. Tseng, D. Zemel, X. Han, and J. Mertz, High-contrast multifocus microscopy with a single camera and z-splitter prism, Optica **7**, 1477 (2020).

[15] T. Vicar, J. Balvan, J. Jaros, F. Jug, R. Kolar, M. Masarik, and J. Gumulec, Cell segmentation methods for label-free contrast microscopy: Review and comprehensive comparison, BMC Bioinf. **20**, 360 (2019).

[16] L. Novotny, R. D. Grober, and K. Karrai, Reflected image of a strongly focused spot, Opt. Lett. **26**, 789 (2001).

[17] S. A. Alexandrov, T. R. Hillman, and D. D. Sampson, Spatially resolved Fourier holographic light scattering angular spectroscopy, Opt. Lett. **30**, 3305 (2005).

[18] S. H. Lee, Y. Roichman, G. R. Yi, S. H. Kim, S. M. Yang, A. van Blaaderen, P. van Oostrum, and D. G. Grier, Characterizing and tracking single colloidal particles with video holographic microscopy, Opt. Express **15**, 18275 (2007).

[19] F. C. Cheong, P. Kasimbeg, D. B. Ruffner, E. H. Hlaing, J. M. Blusewicz, L. A. Philips, and D. G. Grier, Holographic characterization of colloidal particles in turbid media, Appl. Phys. Lett. **111**, 153702 (2017).

[20] B. J. Krishnatreya, A. Colen-Landy, P. Hasebe, B. A. Bell, J. R. Jones, A. Sunda-Meya, and D. G. Grier, Measuring Boltzmann's constant through holographic video microscopy of a single colloidal sphere, Am. J. Phys. **82**, 23 (2014).

[21] B. Ovryn and S. H. Izen, Imaging of transparent spheres through a planar interface using a high-numerical-aperture optical microscope, J. Opt. Soc. Am. A **17**, 1202 (2000).

[22] F. C. Cheong, K. Xiao, D. J. Pine, and D. G. Grier, Holographic characterization of individual colloidal spheres' porosities, Soft Matter **7**, 6816 (2011).

[23] A. Wang, T. G. Dimiduk, J. Fung, S. Razavi, I. Kretzschmar, K. Chaudhary, and V. N. Manoharan, Using the discrete dipole approximation and holographic microscopy to measure rotational dynamics of non-spherical colloidal particles, J. Quant. Spectrosc. Radiat. Transf. **146**, 499 (2014).

[24] K. Snyder, R. Quddus, A. D. Hollingsworth, K. Kirshenbaumb, and D. G. Grier, Holographic immunoassays:

Direct detection of antibodies binding to colloidal spheres, Soft Matter **16**, 10180 (2020).
[25] B. Leahy, R. Alexander, C. Martin, S. Barkley, and V. N. Manoharan, Large depth-of-field tracking of colloidal spheres in holographic microscopy by modeling the objective lens, Opt. Express **28**, 1061 (2020).
[26] L. Mandel and E. Wolf, *Optical Coherence and Quantum Optics* (Cambridge University Press, 1995).
[27] P. Török, P. Varga, Z. Laczik, and G. R. Booker, Electromagnetic diffraction of light focused through a planar interface between materials of mismatched refractive indices: An integral representation, J. Opt. Soc. Am. A **12**, 325 (1995).
[28] A. J. Devaney and E. Wolf, Multipole expansions and plane wave representations of the electromagnetic field, J. Math. Phys. **15**, 234 (1974).
[29] H. Weyl, Ausbreitung elektromagnetischer Wellen über einem ebenen Leiter, Ann. Phys. **365**, 481 (1919).
[30] K. Y. Bliokh, F. J. Rodríguez-Fortuño, F. Nori, and A. V. Zayats, Spin-orbit interactions of light, Nat. Photonics **9**, 796 (2015).
[31] C. Schwartz and A. Dogariu, Conservation of angular momentum of light in single scattering, Opt. Express **14**, 8425 (2006).
[32] M. Born and E. Wolf, *Principles of Optics: Electromagnetic Theory of Propagation, Interference and Diffraction of Light* (Elsevier, 2013).
[33] P. A. Bobbert and J. Vlieger, Light scattering by a sphere on a substrate, Physica A **137**, 209 (1986).
[34] R. S. Dutra, P. A. Maia Neto, H. M. Nussenzveig, and H. Flyvbjerg, Theory of optical-tweezers forces near a plane interface, Phys. Rev. A **94**, 053848 (2016).
[35] C. F. Bohren and D. R. Huffman, *Absorption and Scattering of Light by Small Particles* (Wiley, New York, 1983).
[36] A. R. Edmonds, *Angular Momentum in Quantum Mechanics* (Princeton University Press, Princeton, 1957).
[37] R. S. Dutra, N. B. Viana, P. A. Maia Neto, and H. M. Nussenzveig, Absolute calibration of forces in optical tweezers, Phys. Rev. A **90**, 013825 (2014).
[38] F. W. J. Olver, A. B. Olde Daalhuis, D. W. Lozier, B. I. Schneider, R. F. Boisvert, C. W. Clark, B. R. Miller, B. V. Saunders, H. S. Cohl, and M. A. McClain, NIST digital library of mathematical functions, Release 1.0. 25 of 2019-12-15.
[39] N. B. Viana, M. S. Rocha, O. N. Mesquita, A. Mazolli, and P. A. Maia Neto, Characterization of objective transmittance for optical tweezers, Appl. Opt. **45**, 4263 (2006).
[40] https://refractiveindex.info/.
[41] S. H. Jones, M. D. King, and A. D Ward, Determining the unique refractive index properties of solid polystyrene aerosol using broadband Mie scattering from optically trapped beads, Phys. Chem. Chem. Phys. **15**, 20735 (2013).
[42] M. Daimon and A. Masumura, Measurement of the refractive index of distilled water from the near-infrared region to the ultraviolet region, Appl. Opt. **46**, 3881 (2007).
[43] See Supplemental Material at http://link.aps.org/supplemental/10.1103/PhysRevApplied.15.064012 for the Mathematica code to generate the contrast curve.
[44] E. van der Pol, F. A. W. Coumans, A. Sturk, R. Nieuwland, and T. G. van Leeuwen, Refractive index determination of nanoparticles in suspension using nanoparticle tracking analysis, Nano Lett. **14**, 6195 (2014).
[45] R. Kitamura, L. Pilon, and M. Jonasz, Optical constants of silica glass from extreme ultraviolet to far infrared at near room temperature, Appl. Opt. **46**, 8118 (2007).
[46] C. Gutsche, U. F. Keyser, K. Kegler, F. Kremer, and P. Linse, Forces between single pairs of charged colloids in aqueous salt solutions, Phys. Rev. E **76**, 031403 (2007).
[47] D. Ether, L. B. Pires, S. Umrath, D. Martinez, Y. Ayala, B. Pontes, G. R. de S. Araújo, S. Frases, G. L. Ingold, F. S. S. Rosa, N. B. Viana, H. M. Nussenzveig, and P. A. Maia Neto, Probing the Casimir force with optical tweezers, Europhys. Lett. **112**, 44001 (2015).
[48] A. Kundu, S. Paul, S. Banerjee, and A. Banerjee, Measurement of van der Waals force using oscillating optical tweezers, Appl. Phys. Lett. **115**, 123701 (2019).
[49] M. A. Bevan and D. C. Prieve, Direct measurement of retarded van der Waals attraction, Langmuir **15**, 7925 (1999).
[50] B. Pontes, N. B. Viana, L. T. Salgado, M. Farina, V. Moura-Neto, and H. M. Nussenzveig, Cell cytoskeleton and tether extraction, Biophys. J. **101**, 43 (2011).
[51] H. M. Nussenzveig, Cell membrane biophysics with optical tweezers, Eur. Biophys. J. **47**, 499 (2018).
[52] M. Sun, J. S. Graham, B. Hegedüs, F. Marga, Y. Zhang, G. Forgacs, and M. Grandbois, Multiple membrane tethers probed by atomic force microscopy, Biophys. J. **89**, 4320 (2006).
[53] P. Ruef, J. M. B. Pöschl, and O. Linderkamp, Formation and relaxation of erythrocyte membrane tethers in micropipettes, Clin. Hemorheo. Microcirc. **30**, 39 (2004).
[54] B. Pontes, Y. Ayala, A. C. C. Fonseca, F. F. Romão, R. F. Amaral, L. T. Salgado, F. R. Lima, M. Farina, N. B. Viana, V. Moura-Neto, and H. M. Nussenzveig, Membrane elastic properties and cell function, PLoS ONE **8**, e67708 (2013).
[55] B. Pontes, P. Monzo, and N. C. Gauthier, Membrane tension: A challenging but universal physical parameter in cell biology, Semin. Cell Dev. Biol. **71**, 30 (2017).
[56] J. Soares, G. R. de S. Araujo, C. Santana, D. Matias, V. Moura-Neto, M. Farina, S. Frases, N. B. Viana, L. Romão, H. M. Nussenzveig, and B. Pontes, Membrane elastic properties during neural precursor cell differentiation, Cells **9**, 1323 (2020).
[57] A. Upadhyaya and M. P. Sheetz, Tension in tubulovesicular networks of Golgi and endoplasmic reticulum membranes, Biophys. J. **86**, 2923 (2004).
[58] A. Rustom, R. Saffrich, I. Markovic, P. Walther, and H. H. Gerdes, Nanotubular highways for intercellular organelle transport, Science **303**, 1007 (2004).
[59] A. Sartori-Rupp, D. C. Cervantes, A. Pepe, K. Gousset, E. Delage, S. Corroyer-Dulmont, C. Schmitt, J. Krijnse-Locker, and C. Zurzolo, Correlative cryo-electron microscopy reveals the structure of TNTs in neuronal cells, Nat. Commun. **10**, 1 (2019).
[60] A. Roux, G. Koster, M. Lenz, B. Sorre, J. B. Manneville, P. Nassoy, and P. Bassereau, Membrane curvature controls dynamin polymerization, Proc. Natl. Acad. Sci. U. S. A. **107**, 4141 (2010).
[61] S. Inoue, *Video Microscopy* (Springer Science and Business Media, 2013).

[62] See Supplemental Material at http://link.aps.org/supplemental/10.1103/PhysRevApplied.15.064012 for the video of the defocusing experiment.

[63] I. H. Malitson, Interspecimen comparison of the refractive index of fused silica, J. Opt. Soc. Am. **55**, 1205 (1965).

[64] C. P. Blakemore, A. D. Rider, S. Roy, A. Fieguth, A. Kawasaki, N. Priel, and G. Gratta, Precision Mass and Density Measurement of Individual Optically Levitated Microspheres, Phys. Rev. Appl. **12**, 024037 (2019).

[65] B. T. Draine and P. J. Flatau, Discrete-dipole approximation for scattering calculations, J. Opt. Soc. Am. A **11**, 1491 (1994).

[66] M. A. Yurkin and A. G. Hoekstra, The discrete dipole approximation: An overview and recent developments, J. Quant. Spectrosc. Radiat. Transfer **106**, 558 (2007).

[67] M. A. Yurkin and A. G. Hoekstra, The discrete-dipole-approximation code ADDA: Capabilities and known limitations, J. Quant. Spectrosc. Radiat. Transfer **112**, 2234 (2011).

[68] W. J. Wiscombe, Improved Mie scattering algorithms, Appl. Opt. **19**, 1505 (1980).

[69] S. Yoo and Q.-H. Park, Enhancement of chiroptical signals by circular differential Mie scattering of nanoparticles, Sci. Rep. **5**, 14463 (2015).

[70] J. Karst, Nam H. Cho, H. Kim, H.-E. Lee, K. T. Nam, H. Giessen, and M. Hentschel, Chiral scatterometry on chemically synthesized single plasmonic nanoparticles, ACS Nano **13**, 8659 (2019).

[71] M. Nieto-Vesperinas, *Scattering and Diffraction in Physical Optics* (World Scientific, Singapore, 2006).

Correction: The name of the sixth author appeared incorrectly due to a tagging error and has been fixed.

Second Correction: The previously published Figure 3 contained a misarrangement of panels (j) and (k) and has been fixed.